

Thickness influences on nanostructured MnO thin films, physical properties and sensing performance

A. M. Jabbar^a, E. H. Hadi^b, S. S. Chiad^b, N. F. Habubi^{c,d,*}, K. N. Hussein^e,
Y. H. Kadhim^f, M. Jadan^{g,h}

^aDepartment of Physics, College of Science, Mustansiriyah University, Iraq

^bDepartment of Physics, College of Education, Mustansiriyah University, Iraq

^cDepartment of Radiology and Sonar Techniques, Alnukhba University
College, Baghdad 10013, Iraq

^dDepartment of Radiology Techniques, Al-Qalam University College, Kirkuk
36001, Iraq

^eDepartment of Radiology, Al-Manara College for Medical Science, Iraq

^fDepartment of Optics Techniques, College of Health and Medical Techniques,
AL-Mustaqbal University, Babylon, Hillah, 51001, Iraq.

^gDepartment of Physics, College of Science, Imam Abdulrahman Bin Faisal
University, P.O. Box 1982, 31441 Dammam, Saudi Arabia

^hBasic and Applied Scientific Research Center, Imam Abdulrahman Bin Faisal
University, P.O. Box 1982, 31441 Dammam, Saudi Arabia

This work employed the chemical bath deposition (CBD) technique to fabricate a thin layer of nanostructured MnO. According to XRD measurements, the films have a cubic crystal structure and are polycrystalline, with orientations of (111, 200, 311, and 222), with (200) being the preferred orientation. Although the dislocation density parameters (100.46 to 80.36) and strain decreased from 34.75 to 31.08 and 34.75 to 100.36, respectively, the grain size was largest at (200) nm film thickness and lowest at (300) nm thickness. The deposited films exhibited a smooth surface topography as evidenced by the average surface roughness dropping from 8.70 nm to 4.27 nm, the average particle size observed to be 82.8 nm to 39.2 nm, and a reduction in root mean square (rms) values from 6.82 nm to 3.09 nm in the AFM images. Nanostructured MnO films exhibit a variety of grain morphologies, polycrystalline structure, and uniformity in SEM images. Their optical properties were measured in the 300–900 nm wavelength range. The extinction coefficient ranged from 0.368 to 0.276, whereas the computed refractive indices of the films with varying thicknesses fell between 3.6 and 2.95. The transmittance ranged between 86 and 81% in the VIS-NIR region with a band gap between 3.24 and 3.13 eV, and it was found that the absorption and absorption coefficient increased with film thickness. The thickness of MnO reduces its sensitivity to H₂S gas.

(Received March 20, 2024; Accepted June 19, 2024)

Keywords: MnO, Thin films, Thickness, Bath deposited method, Structural properties, Morphological, Optical, Energy gap

1. Introduction

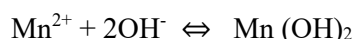
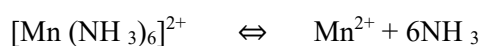
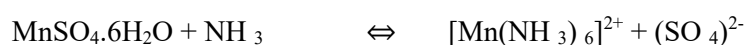
Researchers and businesses have become interested in nanostructured transition metal oxide thin films because of their distinctive physical and chemical characteristics [1-3]. Their limited size and high surface-to-volume ratio contribute to their unique features. Manganese oxide is a particularly interesting nanomaterial since it is non-toxic, low-priced, and readily available [4-7]; band gaps for MnO range from 2.4 to 3.6 eV [8, 9]. Thin film semiconductors are widely used and have attracted substantial attention due to their low manufacturing costs [10]. Different methods may be used to synthesize and grow the nanomaterials used in thin films. A substrate can be covered

* Corresponding author: n.fadhil@alnukhba.edu.iq
<https://doi.org/10.15251/DJNB.2024.192.967>

with thin films using various methods, including PLD [11], CBD [12], ALD [13], CVD[14], and others. Research is being done on MnO with different valence states and crystalline forms for use in electrochemical, electrical, catalytic, and other applications [15]. MnO has been manufactured using several different techniques, including thermal evaporation [16], precipitation [17], ALD [18], PLD [19], chemical spray pyrolysis [20], sol-gel [21], molecular beam epitaxy [22], EBD [23], plasma-assisted hydrothermal method [24], and CBD [3, 25] For a variety of reasons, CBD is now generating a lot of attention. First, the precursor substances required to create CBD are readily accessible and reasonably priced. Additionally, it's possible to make consistent, large-area thin films free of pinholes. The deposition temperature is comparatively low (90 °C), another benefit. [3]. This work discusses the effect of thickness on manganese oxide's structural, morphological and optical properties. Chemical Bath Deposited Technique prepared these thin films to characterize the physical and sensing properties.

2. Experimental

CBD process was used to prepare MnO thin films on glass slides. The glass bases were washed in a cleaning solution, rinsed with distilled water, and dried in the air after being degreased in HNO₃ for 48 hours. A surface that has been cleaned and degreased can serve as a nucleation site for forming films, resulting in highly sticky and uniformly deposited films. A reaction bath containing 0.2 M to 1.0 M precipitated MnO. In that sequence, 2 ml to 10 ml of manganese sulfate, 1 ml to 5 ml of 100% ammonia, and 25 ml to 27 ml of water were added, and 20 to 48 hours were given for deposition. The pH ranges from 10 to 13. The application of complexing agents slows the precipitation process and promotes MnO production. Here, the complicated ion production and film deposition process for MnO includes a step-by-step reaction that is:



While Mn²⁺ ions combine with NH₃ in the alkaline medium to create the tetra amine nickel ([Mn(NH₃)₆]²⁺) complex ions, hydrolysis releases hydroxyl ions. The complexes adsorb on the glass, and subsequently, an ionic exchange of reaction OH⁻ ions causes heterogeneous nucleation and growth. This procedure, known as an "ion-by-ion method," led to the deposition of MnO on a glass slide as a thin, homogeneous, and firmly adhering greenish-blue layer. The weighing method was used to determine the film thickness, which was (250, 300, and 350) nm. A Unico UV-2102 PC spectrophotometer with scan intervals of 3 nm, a Philips PW1800 diffractometer, and an Olympus PMG photomicrograph were used to characterize the films after they had been deposited and annealed. The films' structural properties were examined through X-ray diffraction (XRD) using Cu K_α radiation (λ = 1.5406 Å) with a Philips PW-3710 instrument from Holland. Surface physical morphology was obtained through AFM. The films were subjected to scanning electron microscopy (SEM) analysis using a JEOL-JSM-6360 model from Japan, operating at 20 kV. The films' absorbance-transmittance spectra were measured using a Unico UV- 2102 PC double-beam spectrophotometer in the UV, VIS, and NIR areas (between 300 and 900 nm). Gas-sensing experiments were conducted by positioning the sample within a glass test chamber. MnO films were coated with conducting silver paste. Temperature fluctuations were monitored through a sensitive thermocouple placed inside the sealed glass test chamber. The alteration in electrical resistance in the presence of the target gas was quantified using a Keithley 6514 DMM setup. Precise quantities of the target gas were directed over the sample via a regulated flow meter (with a flow rate of 1 L per minute). All evaluations of gas sensitivity were performed at an operational temperature of 150°C.

3. Results and discussion

Manganese oxide's XRD patterns vary depending on thickness, as shown in Figure 1. When the samples of MnO with thicknesses of (200, 250, and 300) nm were examined to determine the crystalline structure of the film, it was discovered that the films have a polycrystalline structure. Additionally, when the results were compared to the standard JCPDS card No. (01-071-1177), it was found that the films have a monoclinic phase. This result is in good accord with [14], where the favored pattern of development was along the planes (111), (200), (311) and (222), and peaks sites was found at ($\theta = 34.42^\circ, 40.83^\circ, 70.24^\circ$ and 73.65°) correspondingly (200) These outcomes are consistent with [26, 27].

The effect of different thicknesses on grain size D was determined using the Sherrer formula [28, 29]:

$$D = \frac{k\lambda}{\beta \cos\theta} \quad (1)$$

where θ is the Bragg diffraction angle, β is the FWHM, and λ is the wavelength of the incident X-ray and $k = 0.9$. The thickness (250 and 300 nm) of the MnO thin films changed the grain size from 9.98 nm predicted for the deposited MnO thin films to 10.60 nm and 11.15 nm, respectively. The increased thickness of thin films caused a drop in the density of nucleation centers, which caused fewer centers to grow, leading to larger grains. [30].

The dislocation density (δ) was gained via the relation [31, 32]:

$$\delta = \frac{1}{D^2} \quad (2)$$

δ decreases from (100.46 to 80.36).

The strain (ϵ) is obtained by employing Eq. 3 [33, 34]:

$$\epsilon = \frac{\beta \cos\theta}{4} \quad (3)$$

The strain parameter's value falls from (34.75 to 31.08). The acquired structural parameters S_{par} are shown in Table 1, which shows that δ and ϵ increase in value as the thickness of thin films rises [35, 36]. Figure (2) plots FWHM, D , and against various thicknesses.

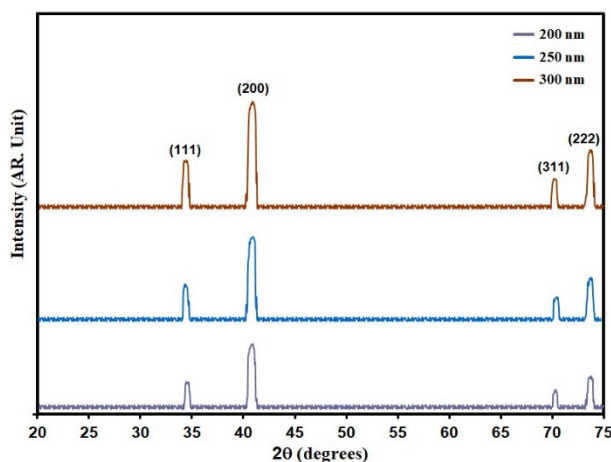
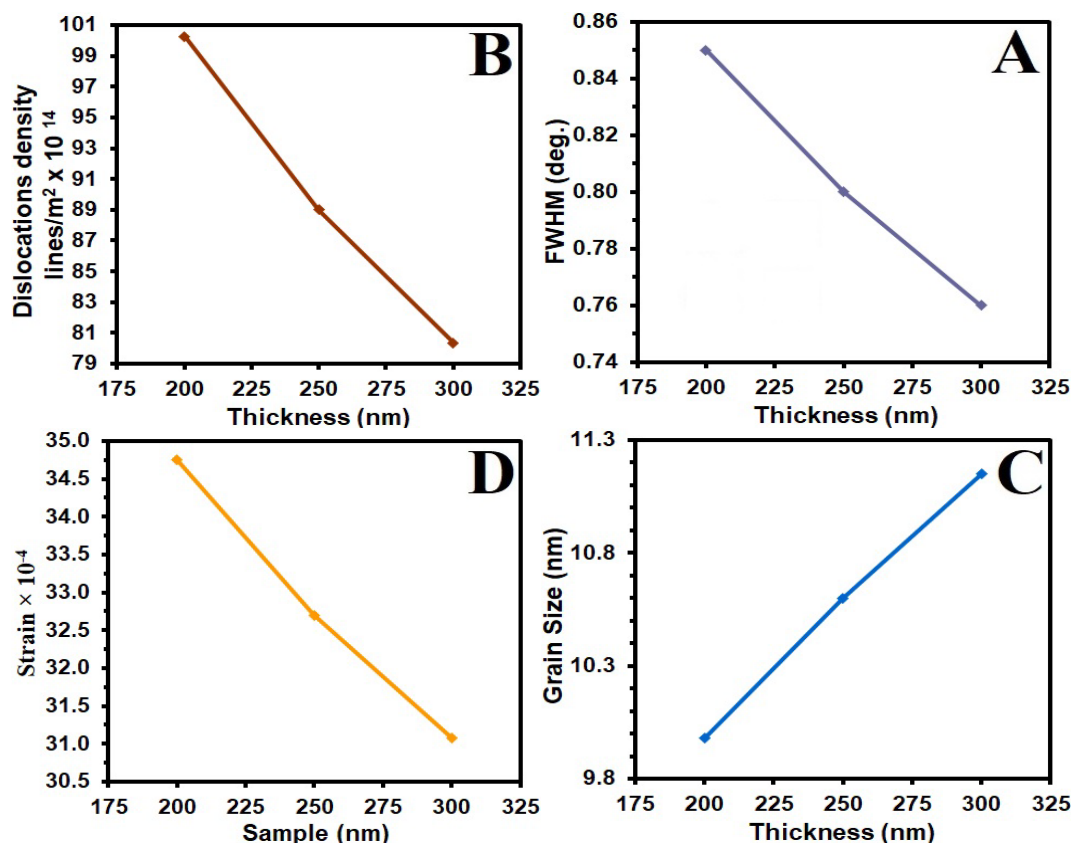


Fig. 1. XRD of MnO film with different thicknesses.

Table 1. XRD analysis results of structural (MnO) thin film with different thicknesses.

Thickness (nm)	2 θ ($^{\circ}$)	(hkl) Plane	FWHM ($^{\circ}$)	Optical bandgap (eV)	Grain size (nm)	Dislocations density ($\times 10^{14}$) (lines/m 2)	Strain ($\times 10^{-4}$)
250	40.83	200	0.85	3.24	9.98	100.46	34.70
300	40.80	200	0.80	3.18	10.60	88.99	32.70
350	40.76	200	0.76	3.13	11.15	80.36	31.08

Fig. 2. FWHM (a) D (b) δ (c) ε (d) of (MnO) thin film with different thicknesses.

The topography of the MnO formed at different thicknesses (200, 250, and 300 nm) is generally depicted in Figure (3). Figure 3 (A₁, A₂, and A₃) displays a 3D picture of the required layer captured by an atomic force microscope. With a decrease in root mean square (rms), AFM images showed a flat surface topography (R_a). The average particle size P_{av} ranged from (82.8 to 39.2) nm in Fig. 3 (C₁, C₂, and C₃), whereas the average surface roughness for the deposited films dropped similarly, from 8.70 nm to 4.27 nm. The AFM parameter P_{AFM} values are shown in Table (2).

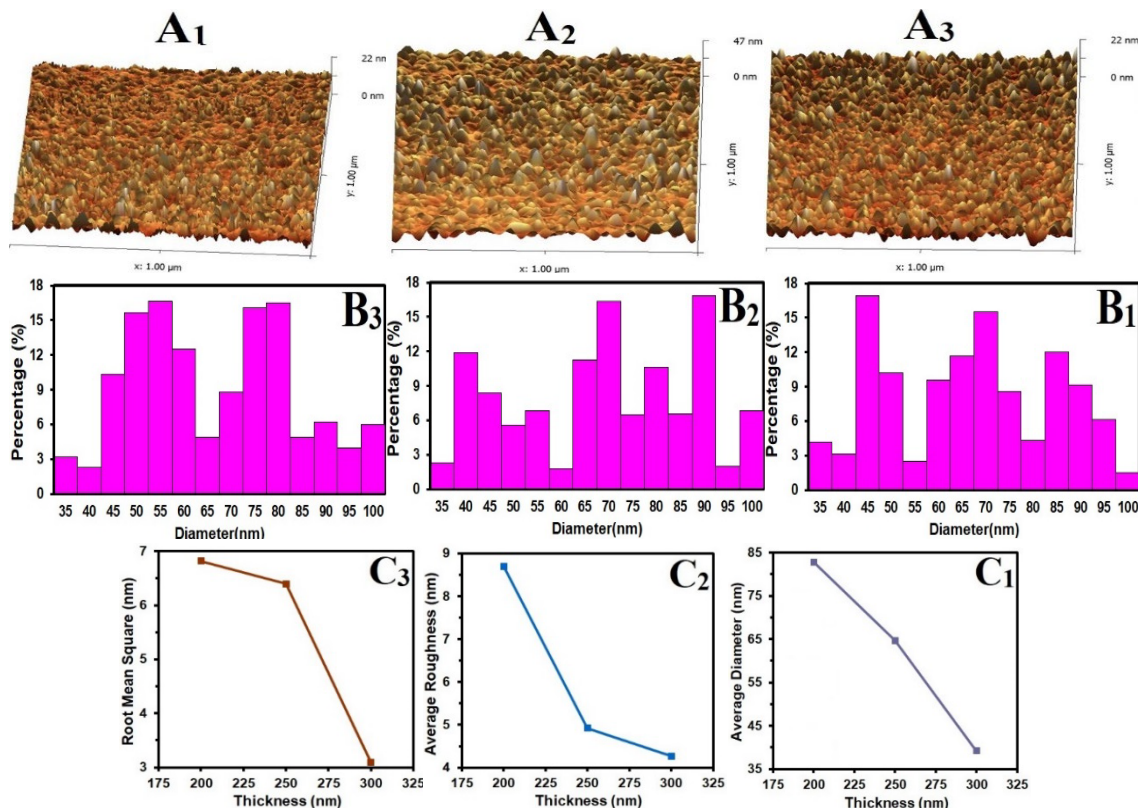


Fig. 3. AFM informations.

Table 2. P_{AFM} of (MnO) thin film with different thicknesses.

Thickness (nm)	P_{av} (nm)	R_a (nm)	rms (nm)
250	82.8	8.70	6.82
300	64.7	4.92	6.40
350	39.2	4.27	3.09

Figure 4 illustrates scanning electron microscopy (SEM) images revealing the surface characteristics of synthesized MnO thin films. The nanostructured thin MnO films exhibit a remarkable homogeneity, displaying a distinct polycrystalline structure with notable surface roughness and tiny pores. No macroscopic defects were observed, such as exfoliation, voids, or holes. Furthermore, Fig. (3) depicts that the grains exhibit diversity in size and shape, manifesting as spherical, lamellar, and various other configurations [20]. The increase in thickness correlates with an augmentation in the size of crystallites within the thin films, resulting in an average grain diameter of approximately 90 nm.

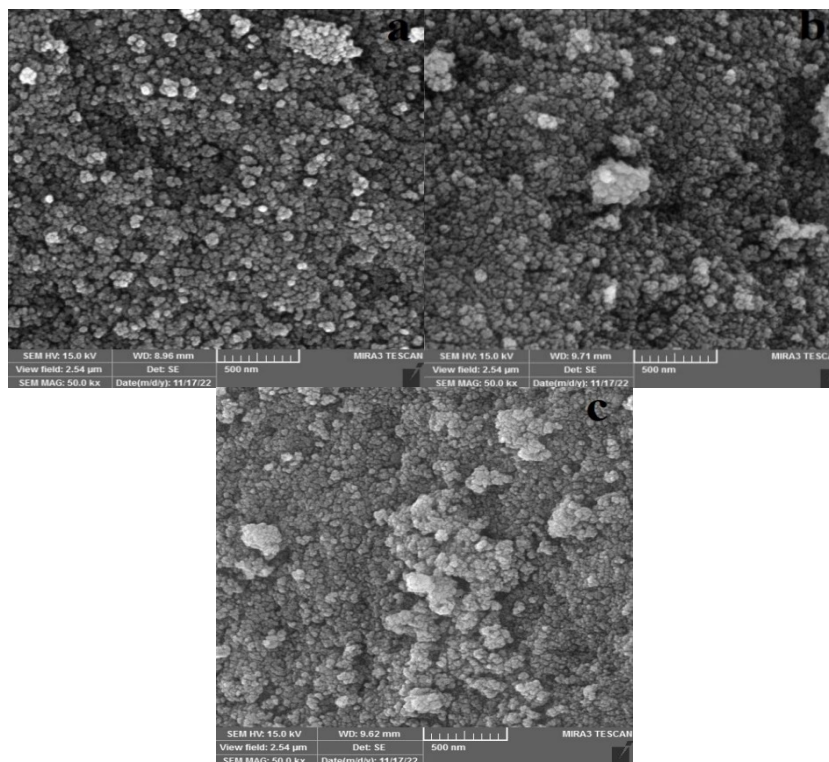


Fig. 4. SEM images of the surface of the MnO thin films deposited at different thicknesses.

Their optical characteristics were assessed across wavelengths. As can be seen from Figure (5), which plots absorbance against wavelength, All of the films with greater thicknesses (250 and 300 nm) displayed low absorbance in the VIS's short wavelength region, which quickly dropped to lower values in the VIS's long wavelength region before progressively declining into the NIR realm. The absorbance of the thinnest film, which was 200 nm, was greater than that of the other films and decreased over time from the short wavelength of the visible spectrum to the near-infrared region. With increasing precursor thicknesses, the MnO films' absorbance decreased, possibly ascribed to an increase in film density [37, 38].

The following formula was used to determine the transmittance of these films, which is shown in Figure (5), from absorbance data: [39, 40]:

$$A = 2 - \log_{10} (\% T) \quad (4)$$

Figure (6) displays the transmission spectra of as-grown films at varied thicknesses (200, 250, and 300) nm from the near ultraviolet to the near-infrared regions. Different film thicknesses can increase crystallinity, as seen by the optical transmission being crisper when the films were at thicknesses of (200 and 300) nm [41, 42]. Additionally, we discovered that all films exhibit strong visible light transmission, allowing MnO thin films formed under identical circumstances in a chemical bath to be actively used as a window material in solar cells. It was discovered that as film thickness grew, transmittances decreased. In the VIS-NIR areas, transmittances ranged between 86 and 81%.

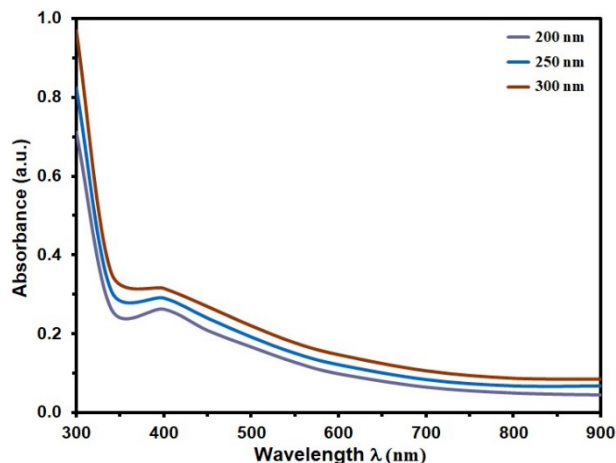


Fig. 5. Absorbance with wavelength of the (MnO) thin film with different thickness.

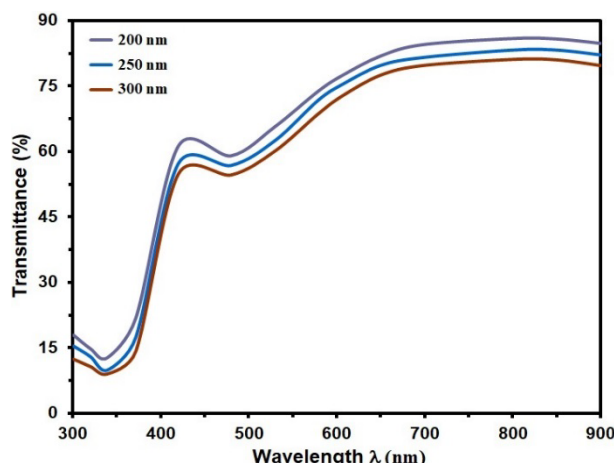


Fig. 6. Transmittance with wavelength of the (MnO) thin film with different thicknesses.

The absorption coefficient α is given by [43, 44]:

$$\alpha = \ln(1/Td) \quad (5)$$

where d is film thickness, the absorption coefficient varied from (0.02 - 0.55) for the energy range (1.0 - 2.5) eV and rose progressively as photon energy increased. However, it did not grow consistently as thickness increased [45]. Figure 7 demonstrates this.

Tauc's relationship of $(\alpha h\nu)^2$ versus photon energy may be used to calculate the band gap energy (E_g) of the MnO (eV) [46, 47]:

$$(\alpha h\nu) = A(h\nu - E_g)^n \quad (6)$$

where n is 0.5 for the direct allowed transition, A stands for the constant band edge sharpening, h for the Planck constant, and $h\nu$ for photon energy. Plotting $(\alpha h\nu)^2$ and extrapolating the linear section of the curve to equal zero allowed for calculating the optical band gap energy. Figure (8) displays the square graph $(h\nu)$ vs photon energy for Tauc's MnO thin film at varied thicknesses (200, 250, and 300 nm) ($h\nu$). The estimated E_g values are between 3.24 and 3.13 eV. The declines in E_g could be caused by a surplus of manganese ions, either interstitial or substitutional, forming new localized levels that penetrate essential levels. [48].

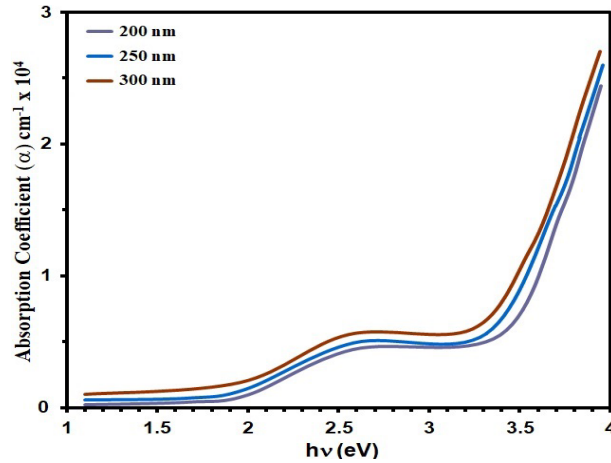


Fig. 7. α Vs $h\nu$ of grown films.

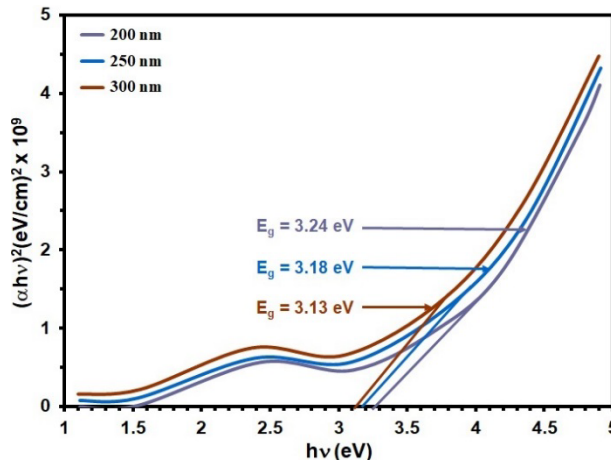


Fig. 8. $(\alpha h\nu)^2$ of the grown films.

Optical constants included extinction coefficient (k) and refractive index (n). The value of k is measured by using the relation [49]:

$$k = \frac{\alpha\lambda}{4\pi} \tag{7}$$

where λ is the wavelength of the radiation striking the film when it is incident. As demonstrated in Fig. (9), the behavior of the extinction coefficient (k) at different thicknesses (200, 250, and 300 nm) is almost identical to that of the corresponding absorption coefficient. These figures show that all films' extinction coefficient generally falls as thickness increases. The thin film's crystallinity may be connected to the decline in extinction coefficient value [22].

The following equation can be used to get the refractive index (n). [50]:

$$n = \left(\frac{1+R}{1-R}\right) + \sqrt{\frac{4R}{(1-R)^2} - k^2} \tag{8}$$

where R is the reflectance, according to Figure 10, the refractive index decreased with increasing thickness and varied from 1.78 to 3.06 for energies between 300 and 900 nm. The refractive indices of the manganese oxide thin films declined exponentially as wavelengths increased between 500 and 850 nm, indicating limited light absorption at extended wavelength ranges. The following equation can be used to get n) [21].

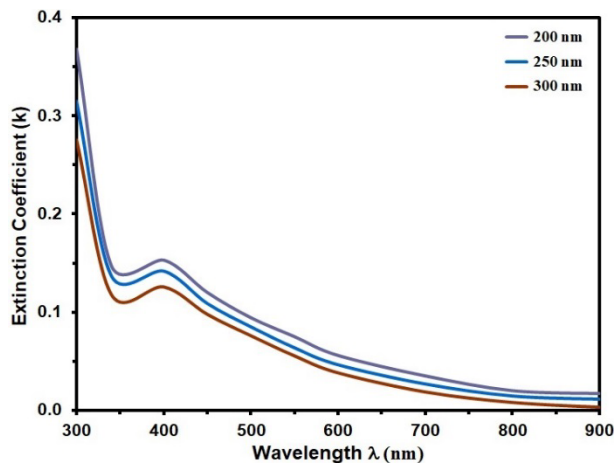


Fig. 9. k of MnO thin film with different thickness.

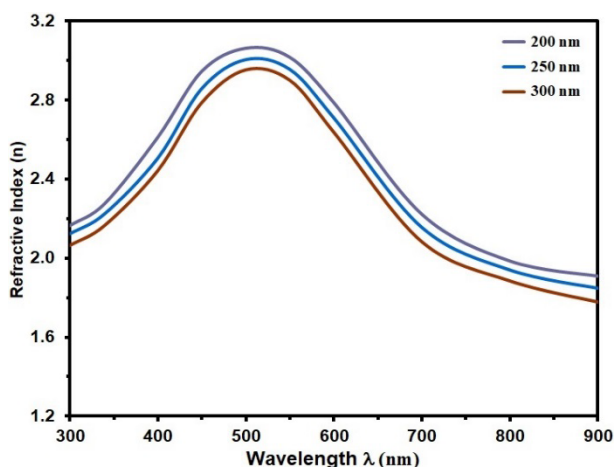


Fig. 10. Refractive Index of MnO thin film with different thicknesses.

The gas sensing capabilities of MnO film were evaluated for H_2S gas at an operating temperature of $150^\circ C$. Response time was determined by exposing a film to 240 ppm H_2S concentrations and recording its resistance over time. The observed trend indicated increased MnO film resistance upon exposure to H_2S gas.

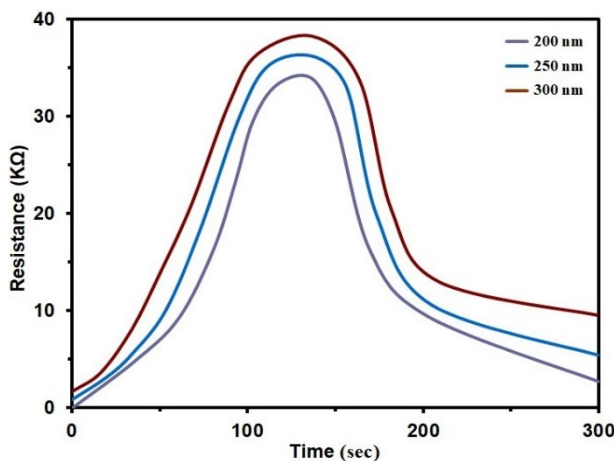


Fig. 11. Resistance via time of MnO thin film with different thicknesses at 240 ppm H_2S

in at the optimum working temperature.

The interpretation of the results would suggest that the resistance of the MnO film increases when exposed to H₂S gas [51]. Fig. (11) illustrates typical gas response curves for MnO films of varying thicknesses (200, 250, and 300 nm).

The detection sensitivity, or sensor response, can be calculated as per equation can be computed as [52]:

$$\text{Sensitivity} = \frac{\Delta R}{R_g} = \left| \frac{R_g - R_a}{R_g} \right| \times 100 \% \quad (9)$$

Fig. (12) shows the sensitivity of MnO films to 80, 160 and 240 ppm of H₂S gas as a function of thicknesses (200, 250, and 300 nm). As evident, the sensitivity decreases with thickness. In other words, thicker films exhibit lower sensitivity to varying concentrations of H₂S. This can be attributed to the gas diffusion characteristics through films. Thicker films may impede the diffusion process, reducing sensitivity [53]. The sensitivity decreases from 28.2% to 3.6% for 240 ppm, 24.1% to 1.8% for 160 ppm, and 21.3% to 0.6% for 80 ppm across the respective thicknesses (200, 250, and 300 nm). The observed decreases in sensitivity percentages for 240 ppm, 160 ppm, and 80 ppm suggest that the thinning of MnO films enhances their responsiveness to H₂S gas at the specified concentrations [54].

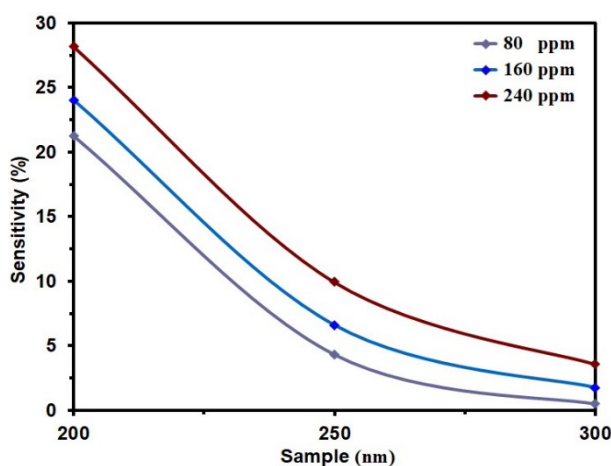


Fig. 12. Sensitivity of MnO thin film with different thicknesses for (80, 160, 240) ppm H₂S in at the optimum working temperature.

4. Conclusion

This paper investigates the impact of manganese oxide's thickness on its structural, morphological, and optical characteristics. According to the XRD pattern, the produced films have a polycrystalline cubic structure. The maximum intensity peak coincides with the ideal orientation (200) for films with a thickness of 300 nm. The strain (%) value falls from 34.75 to 31.08, while the grain size for MnO thin films is around (9.98 -11.15) nm. With film thicknesses of 200 nm and 300 nm, respectively, the AFM picture revealed that average particle sizes were in the range of (82.8 to 39.2) nm, while surface roughness average and root mean square decreased with film thickness. SEM images reveal homogeneous nanostructured MnO films with polycrystalline structures and grain shapes. Thicker films (300 nm) exhibit predominant cubic-like crystallites. The UV-Vis in the (300-900 nm) wavelength region was used to conduct optical investigations on the films, including absorption, transmittance, absorption coefficient, band gap energies, refractive index and Extinction coefficient. MnO film senses H₂S gas at 150°C, increasing resistance at 240 ppm. Sensitivity diminishes with increasing thickness.

Acknowledgements

The authors would like to acknowledge the support of Mustansiriya University (www.uomustansiriya.edu.iq).

References

- [1]. J. Ma, G. K. Chuah, S. Jaenicke, R. Gopalakrishnan, K. L. Tan, *Phys. Chem. Chem. Phys.*, 100, 585 – 593 (1996); <https://doi.org/10.1002/bbpc.19961000509>
- [2] H. Ahmadian, F.S. Tehrani, M. Aliannezhadi, *Mater Res Express* ,6(10),105024 (2019); <https://scholarbank.nus.edu.sg/handle/10635/75697>
- [3] B. Astinchap, R. Moradian, T. Namdari, S. Jurečka, Ş. Țălu, *Optical Quantum Electron*, 51(6),170 (2019); <https://doi.org/10.1007/s11082-019-1891-z>
- [4] M. Jamali, F. S Tehrani, *Mater Sci Semiconductor Process*, 107,104829 (2020); <https://doi.org/10.1016/j.mssp.2019.104829>
- [5] A. A. Abdul Razaq , F. H. Jasim , S. S. Chiad , F. A. Jasim, Z. S. A. Mosa , Y. H. Kadhimd, *Journal of Ovonic Research*, 20 (2), 131 – 141 (2024); <https://doi.org/10.15251/JOR.2024.202.131>
- [6] F. A. Jasima , Z. S. A. Mosa, N. F. Habubi, Y. H. Kadhim, S. S. Chiad, *Digest Journal of Nanomaterials and Biostructures*, 18 (3), 1039–1049 (2023); <https://doi.org/10.15251/DJNB.2023.183.1039>
- [7] S. H. Bea,, S. Y. Lee, B. J. Jin, S. Im, *Applied Surface Science*, 169 -170, 525-528 (2001); [https://doi.org/10.1016/S0169-4332\(00\)00752-2](https://doi.org/10.1016/S0169-4332(00)00752-2)
- [8] S. K. Muhammad, M. O. Dawood, N. Y. Ahmed, E. S. Hassan, N. F. Habubi, S. S. Chiad, *Journal of Physics: Conference Series*, 1660 (1), 012057 (2020); <https://doi.org/10.1088/1742-6596/1660/1/012057>
- [9] R. Naeem, R. Yahya,, A. Pandikumar, N. M. Huang, M. Arifin, Z. Misran, M. Mazhar, *Materials Today Communications*, 4, 141–148 (2015); <https://doi.org/10.1016/j.mtcomm.2015.06.004>
- [10] H. Zhu, J. Zhang, C. Li, F. Pan, T. Wang, B. Huang, *Thin Solid Films*, 517, 5700–5704 (2009); <https://doi.org/10.1016/j.tsf.2009.02.127>
- [11] F. H. Jasim, H. R. Shakir, S. S. Chiad, N. F. Habubi, Y. H. Kadhi,, Jadan, M., *Digest Journal of Nanomaterials and Biostructures*, 18(4), 1385–1393 (2023); <https://doi.org/10.15251/DJNB.2023.184.1385>
- [12] O., Nilsen, H. Fjellvag, A. Kjekshus, *Thin Solid Films*, 444, 44-51 (2003); [https://doi.org/10.1016/S0040-6090\(03\)01101-5](https://doi.org/10.1016/S0040-6090(03)01101-5)
- [13] H. Unuma, T. Kanehama, K. Yamamoto, K. Watanabe, T. Ogata, M. Sugawara, *Journal of Materials Science*, 38,255-259 (2003); <https://doi.org/10.1023/A:1021197029004>
- [14] S. Ching, S. M. Hughes, T. P. Gray, E. J. Welch, *Microporous and Mesoporous Materials* 76: 41-49 (2004); <https://doi.org/10.1016/j.micromeso.2004.07.031>
- [15] S.-C. Pang, M. A. Anderson, T. W. Chapman, *J. Electrochem. Soc.*, 147, 444–450 (2000); <https://doi.org/10.1149/1.1393216>
- [16] A. A. Dakhel, *Thin Solid Films.*, 496, 353-359 (2006); <https://doi.org/10.1016/j.tsf.2005.09.024>
- [17] V. Subramanian, H. Zhu, and B. Wei, *Chemical Physics Letters*, 453 (4–6), 242–249 (2008); <https://doi.org/10.1016/j.cplett.2008.01.042>
- [18] O. Nilsen, H. Fjellva°g, A. Kjekshus, *Thin Solid Films*, 444, 44–51 (2003); [https://doi.org/10.1016/S0040-6090\(03\)01101-5](https://doi.org/10.1016/S0040-6090(03)01101-5)
- [19] W. Neubeck, L. Ranno, M.B. Hunt, C. Vettier, D. Givord, *Appl. Surf. Sci.*, 138-139, 195-198 (1999); [https://doi.org/10.1016/S0169-4332\(98\)00421-8](https://doi.org/10.1016/S0169-4332(98)00421-8)
- [20] M. E. Raja, S. G. Victoriab, V. BenaJothyb, C. Ravidhasc, J. Wollschlägerd, M. Suendorfd, M. Neumannd, M. Jayachandrane, C. Sanjeevi-rajaf, *Appl. Surf.Sci.*, 256, 2920–2926 (2010); <https://doi.org/10.1016/j.apsusc.2009.11.051>

- [21] C. Y. Chen, S. C. Wang, Y. H. Tien, W. T. Tsai, C. K. Lin, *Thin Solid Films*, 518, 1557–1560 (2009); <https://doi.org/10.1016/j.tsf.2009.09.072>
- [22] L. Ren, S. Wu, W. Zhou, S. Li, *J. Cryst. Growth*, 389, 55–59 (2014); <https://doi.org/10.1016/j.jcrysgro.2013.11.085>
- [23] O. Erlandsson, J. Lindvall, N.N. Toan, N.V. Hung, V.T. Bich, N. N. Dinh, *Phys. Status Solidi (a)*, 139, 451457 (1993); <https://doi.org/10.1002/pssa.2211390218>
- [24] D. Yan, P. Yan, S. Cheng et al., *Cryst. Growth. Des.*, 9, 218–222 (2009); <https://doi.org/10.1021/cg800312u>
- [25] H.Y. Xu, S.L. Xu, X.D. Li, H. Wang, *Appl. Surf. Sci.*, 252, 4091–4096 (2006); <https://doi.org/10.1016/j.apsusc.2005.06.011>
- [26] A. S. Al Rawas, M. Y. Slewa, B. A. Bader, N. F. Habubi, S. S. Chiad, *Journal of Green Engineering*, 10 (9), 7141-7153 (2020); <https://doi.org/10.1021/acsami.1c00304>
- [27] R. S. Ali, H. S. Rasheed, N. F. Habubi, S.S. Chiad, *Chalcogenide Letters*, 20 (1), 63–72 (2023); <https://doi.org/10.15251/CL.2023.201.63>
- [28] K. Y. Qader, R. A. Ghazi, A. M. Jabbar, K. H. Abass, S. S. Chiad, *Journal of Green Engineering*, 10 (10), 7387-7398 (2020); <https://doi.org/10.1016/j.jece.2020.104011>
- [29] A. Ghazai, K. Qader, N. F. Hbubi, S. S. Chiad, O. Abdulmunem, *IOP Conference Series: Materials Science and Engineering*, 870 (1), 012027 (2020); <https://doi.org/10.1088/1757-899X/870/1/012027>
- [30] B. A. Bader, S. K. Muhammad, A. M. Jabbar, K. H. Abass, S. S. Chiad, N. F. Habubi, *J. Nanostruct.*, 10(4): 744-750, (2020); <https://doi.org/10.22052/JNS.2020.04.007>
- [31] O. M. Abdulmunem, A. M. Jabbar, S. K. Muhammad, M. O. Dawood, S. S. Chiad, N. F. Habubi, *Journal of Physics: Conference Series*, 1660 (1), 012055 (2020); <https://doi.org/10.1088/1742-6596/1660/1/012055>
- [32] E. H. Hadi, M. A. Abbsa, A. A. Khadayeir, Z. M. Abood, N. F. Habubi, and S.S. Chiad, *Journal of Physics: Conference Series*, 1664 (1), 012069 (2020); <https://doi.org/10.1088/1742-6596/1664/1/012069>
- [33] R. I. Jasim, E. H. Hadi, S. S. Chiad, N. F. Habubi, M. Jadan, J. S. Addasi, *Journal of Ovonic Research*, 19 (2), 187 – 196 (2023)..
- [34] H.T. Salloom, R. I. Jasim, N. F. Habubi, S. S. Chiad, M. Jadan, J. S. Addasi, *Chinese Physics*, 30 (6), 068505 (2021); <https://doi.org/10.1088/1674-1056/abd2a7>
- [35] K. Y. Qader, E. H. Hadi, N. F. Habubi, S. S. Chiad, M. Jadan, J. S. Addasi, *International Journal of Thin Films Science and Technology*, 10 (1), 41-44 (2021); <https://doi.org/10.18576/ijfst/100107>
- [36] H. T. Salloom, E. H. Hadi, N. F. Habubi, S. S. Chiad, M. Jadan, J. S. Addasi, *Digest Journal of Nanomaterials and Biostructures*, 15 (4), 189-1195 (2020); <https://doi.org/10.15251/DJNB.2020.154.1189>
- [37] R. S. Ali, N. A. H. Al Aaraji, E. H. Hadi, N. F. Habubi, S. S. Chiad, *Journal of Nanostructures* this link is disabled, 10(4), 810–816 (2020); <https://doi.org/10.22052/jns.2020.04.014>
- [38] A. A. Khadayeir, R. I. Jasim, S. H. Jumaah, N. F. Habubi, S. S. Chiad, *Journal of Physics: Conference Series*, 1664 (1) (2020); <https://doi.org/10.1088/1742-6596/1664/1/012009>
- [39] S. S. Chiad, A. S. Alkelaby, K. S. Sharba, *Journal of Global Pharma Technology*, 11 (7), 662-665, (2020); <https://doi.org/10.1021/acscatal.1c01666>
- [40] Chiad, S.S., Noor, H.A., Abdulmunem, O.M., Habubi, N.F., *Journal of Physics: Conference Series* 1362(1), 012115 (2019); <https://doi.org/10.1088/1742-6596/1362/1/012115>
- [41] R. S. Ali, M. K. Mohammed, A. A. Khadayeir, Z. M. Abood, N. F. Habubi and S. S. Chiad, *Journal of Physics: Conference Series*, 1664 (1), 012016 (2020); <https://doi.org/10.1088/1742-6596/1664/1/012016>
- [42] N. N. Jandow, M. S. Othman, N. F. Habubi, S. S. Chiad, K. A. Mishjil, I. A. Al-Baidhany, *Materials Research Express*, 6 (11), (2020); <https://doi.org/10.1088/2053-1591/ab4af8>
- [43] M. S. Othman, K. A. Mishjil, H. G. Rashid, S. S. Chiad, N. F. Habubi, I. A. Al-Baidhany, *Journal of Materials Science: Materials in Electronics*, 31(11), 9037-9043 (2020); <https://doi.org/10.1007/s10854-020-03437-0>

- [44] E. S. Hassan, K. Y. Qader, E. H. Hadi, S. S. Chiad, N. F. Habubi, K. H. Abass, *Nano Biomedicine and Engineering*, 12(3), 205-213 (2020); <https://doi.org/10.5101/nbe.v12i3.p205-213>
- [45] E. H. Hadi, D. A. Sabur, S. S. Chiad, N. F. Habubi, K., Abass, *Journal of Green Engineering*, 10 (10), 8390-8400 (2020); <https://doi.org/10.1063/5.0095169>
- [47] K. S. Sharba, A. S. Alkelaby, M. D. Sakhil, K. H. Abass, N. F. Habubi, S. S. Chiad, Enhancement of urbach energy and dispersion parameters of polyvinyl alcohol with Kaolin additive, *NeuroQuantology*, 18 (3), 66-73 (2020); <https://doi.org/10.14704/NQ.2020.18.3.NQ20152>
- [48] M. D. Sakhil, Z. M. Shaban, K. S. Sharba, N. F. Habub, K. H. Abass, S. S. Chiad, A. S. Alkelaby, *NeuroQuantology*, 18 (5), 56-61 (2020); <https://doi.org/10.14704/nq.2020.18.5.NQ20168>
- [49] Khadayeir, A. A., Hassan, E. S., Mubarak, T. H., Chiad, S.S., Habubi, N. F., Dawood, M.O., Al-Baidhany, I. A., *Journal of Physics: Conference Series*, 1294 (2) 022009(2019); <https://doi.1088/1742-6596/1294/2/022009>
- [50] N. Y. Ahmed, B. A. Bader, M. Y. Slewa, N. F. Habubi, S. S. Chiad, *NeuroQuantology*, 18(6), 55-60 (2020); <https://doi.org/10.1016/j.jlumin.2021.118221>
- [51] A. J. Ghazai, O. M. Abdulmunem, K. Y. Qader, S. S. Chiad, N. F. Habubi, *AIP Conference Proceedings* 2213 (1), 020101 (2020); <https://doi.org/10.1063/5.0000158>
- [52] H. A. Hussin, R. S. Al-Hasnawy, R. I. Jasim, N. F. Habubi, S. S. Chiad, *Journal of Green Engineering*, 10(9), 7018-7028 (2020); <https://doi.org/10.1088/1742-6596/1999/1/012063>
- [53] S. S. Chiad, H. A. Noor, O. M. Abdulmunem, N. F. Habubi, M. Jadan, J. S. Addasi, *Journal of Ovonic Research*, 16 (1), 35-40 (2020). <https://doi.org/10.15251/JOR.2020.161.35>
- [54] R. J. Ramalingam, H. Al-Lohedan, A. M. Tawfik, G. Periyasamy, M. R. Muthumareeswaran, *Chalcogenide Lett.*, 17, 423-428 (2020); <https://doi.org/10.15251/CL.2020.178.423>